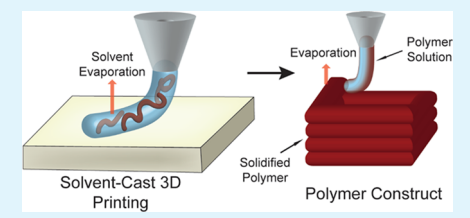
Additive Manufacturing of Mechanically Isotropic Thin Films and Membranes via Microextrusion 3D Printing of Polymer Solutions

Manjot Singh,[†] Alexander P. Haring,^{†,‡} Yuxin Tong,[†] Ellen Cesewski,^{†,§} Edwin Ball,[⊥] Ross Jasper,[⊥] Eric M. Davis,[⊥] and Blake N. Johnson*,^{†,‡,§,}∥_☉

Supporting Information

ABSTRACT: Polymer extrusion additive manufacturing processes, such as fused filament fabrication (FFF), are now being used to explore the fabrication of thin films and membranes. However, the physics of molten polymer extrusion constrains achievable thin film properties (e.g., mechanical isotropy), material selection, and spatial control of film composition. Herein, we present an approach for fabrication of functional polymer thin films and membranes based on the microextrusion printing of polymer solutions, which we refer to as "solvent-cast printing" (SCP). Constructs fabricated via SCP exhibited a 43% reduction in



anisotropy of tensile strength relative to those fabricated using FFF. The constructs fabricated via SCP exhibited a lesser extent of visible layering defects relative to those fabricated by FFF. Further, the swelling dynamics of the films varied depending on the membrane fabrication technique (i.e., SCP vs manual drop casting). The opportunity for expanding material selection relative to FFF processes was demonstrated by printing poly(benzimidazole), a high-performance thermoplastic with high glasstransition temperatures ($T_g \sim 400$ °C). Results from this work indicate that our new approach could facilitate the manufacture of mechanically isotropic thin films and membranes using currently unprintable high-performance thermoplastics.

KEYWORDS: 3D printing, thin films, membranes, solvent casting, drop casting

INTRODUCTION

Polymer thin films (e.g., membranes and coatings) are ubiquitous across manufacturing processes. For example, polymer thin films are used for a variety of applications, including, but not limited to, scaffolds for tissue engineering, functional materials for sensing, coatings for biomedical and electronic devices, and membrane-based separation technologies. Polymer membranes are used across a range of separation processes, whereas polymer coatings are used within both destructive-based micro- and nanofabrication processes as well as surface property modification postprocessing steps. Polymer coatings can be deposited using dry or wet processes, such as chemical vapor deposition and casting, respectively. Although dry processes have the advantage of providing coatings to three-dimensional (3D) objects, wet processes have various advantages regarding material selection. For example, wet processes are compatible with a range of high-performance polymers and provide the ability to integrate dispersed phases, such as nanomaterials, for creation of thin film composites.^{2,3} Although a variety of wet processes exist for depositing polymer thin films, such as drop casting, 4,5 dip coating, 6,7 and spin coating, 8–10 they exhibit limitations regarding the fabrication of multilayered thin films and control over thin film spatial composition and properties.

Multilayered polymer constructs can be 3D printed using a variety of additive manufacturing (AM) processes, including stereolithography, 11-19 jetting, 18-20 and microextrusion, 18,19 which differ in resolution, material compatibility, and speed. For example, stereolithography offers high resolution as a lightdriven process¹⁷ but limits material selection and multimaterial integration capability because of the requirement that materials be photocurable with sufficient polymerization kinetics and refractive indices needed for cross-linking in a liquid bath of precursor. As a result, polymer synthesis and design for stereolithography processes are active research areas. 12,14 In addition to laser-based processes, extrusion-based processes, commonly referred to as jetting and microextrusion printing, have received considerable attention for polymer 3D printing. Whereas jetting processes offer flexibility in dispensing parameters²¹ and the ability to fabricate parts with microstructural and topographical features on the scale of tens to hundreds of micrometers,²² they are limited regarding material selection because of the requirement that the fluid exhibit suitable viscosities and surface tension for droplet formation and extrusion through a small diameter nozzle without clogging. 19,20 Alternatively, microextrusion processes offer the widest range of material compatibility and multimaterial integration capabilities and similar resolution to jetting.²³

Received: December 19, 2018 Accepted: January 16, 2019

Published: January 31, 2019



[†]Department of Industrial and Systems Engineering, [‡]Macromolecules Innovation Institute, [§]Department of Materials Science and Engineering, and Department of Chemical Engineering, Virginia Tech, Blacksburg, Virginia 24061, United States

¹Department of Chemical and Biomolecular Engineering, Clemson University, Clemson, South Carolina 29634, United States

Although microextrusion 3D printing of molten polymers, referred to as fused filament fabrication (FFF), ^{18,19} is an attractive approach for fabricating thin films and membranes, ²⁴ the physics of polymer extrusion constrains the achievable material properties (e.g., isotropy), ^{25–27} material selection, ^{28,29} and resolution. ³⁰ Thus, a low-temperature microextrusion printing process for fabrication of thin films and membranes could advance polymer AM, particularly regarding the fabrication of spatially programmed multimaterial thin films and membranes.

Although many polymers have been 3D printed using FFF, 31,32 the need to melt the polymer restricts the selection of candidate polymers.³³ First, polymers for FFF must exhibit sufficiently low melting or flow temperature to facilitate extrusion and avoid thermal degradation. This constraint can restrict the use of high-performance thermoplastics because of their high flow or melt temperatures. Second, polymers must be preprocessed into filaments for extrusion, which restricts the polymer mechanical properties. Third, the rheological properties of molten polymers relative to polymer solutions limit the minimum achievable nozzle size. Fourth, the solidification of printed parts via cooling limits the achievable part quality because of interlayer re-welding effects^{27,34,35} that result in anisotropic mechanical properties. 25,26 Thus, the mechanical behavior of 3D printed polymers has been widely investigated. 31,33,35,36 Although existing approaches for solving such technical challenges are being examined in the form of multimaterial thermoplastic systems (e.g., composites), 33,37,38 the use of height-dependent raster orientations, 39 systematic testing of process parameters via design of experiment approaches, ²⁵ and study of process-structure-property relationships (e.g., via spatiotemporal heat transfer simulations),³⁶ they remain focused on high-temperature material extrusion and assembly. Thus, low-temperature microextrusion processes that enable the printing of polymer solutions could expand the material set for polymer thin film and membrane AM and improve the quality of thin films and membranes relative to those fabricated using FFF. For example, precipitation- and coagulation-based solution printing approaches have facilitated the fabrication of microscale constructs.40,41

Here, we show a new approach for polymer AM based on the microextrusion printing of polymer solutions, referred to as "solvent-cast printing" (SCP). Experimental and computational studies revealed that microextrusion printing of polymer solutions enables the fabrication of robust thin films and membranes using commonly printed thermoplastics and highperformance thermoplastics that have not yet been printed. Our results suggest that AM via microextrusion of polymer solutions relaxes the material property requirements relative to jetting processes, given the process does not require droplet formation or utilize a periodic driving force. Material testing and characterization studies on the printed test specimens showed that the constructs fabricated via SCP exhibited a 43% reduction in anisotropy of tensile strength relative to those fabricated from molten polymers. In addition, the relaxation (or swelling) dynamics of the hydrated SCP films were faster than those measured for manually drop-cast membranes. Scanning electron microscopy (SEM) studies showed that the samples fabricated via SCP and FFF exhibited different microstructures at the layer interfaces. Effects of the process parameters on the evaporation-driven solidification process (e.g., solvent vapor pressure) were modeled using a twodimensional moving boundary transient mass transfer model. New opportunities for expanded material selection in polymer AM were demonstrated by printing of a high-performance polymer that cannot be processed by FFF 3D printing systems, poly(benzimidazole) (PBI). Overall, these results suggest that microextrusion printing of polymer solutions offers an attractive process for facile fabrication of functional thin films and membranes using currently unprintable high-performance thermoplastics.

■ RESULTS AND DISCUSSION

Microextrusion Printing of Polymer Solutions and Comparison of Part Quality to FFF Processes. As shown in Figure 1, SCP is based on continuous extrusion of a polymer

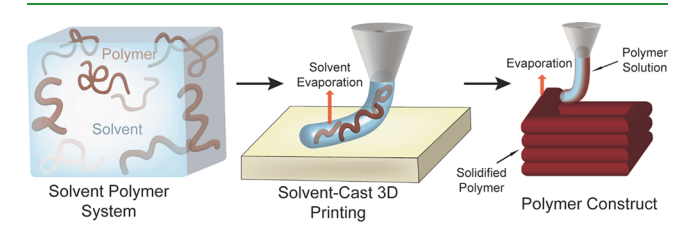


Figure 1. Schematic of polymer solution microextrusion printing in which a polymer—solvent system is continuously extruded as the extruder moves along a specified tool path (i.e., a robotic-directed casting process). The printed polymer solution solidifies due to evaporation of the solvent allowing for fabrication of thin films and membranes.

solution from a nozzle, whereby the extruded material subsequently solidifies due to solvent evaporation. The principle is similar to that of direct-write applications of colloidal inks yet relaxes the constraint of having a high volume fraction of the solid component in the ink. As poly(lactic acid) (PLA) is one of the most commonly used materials for FFF, it was used here as a test material to examine the quality of SCP relative to established polymer AM processes. As shown in Figure 2a, SCP was used to print PLA tensile test specimens using a 30 wt % polymer solution in chloroform.

Figure 2b,c shows the tensile testing results obtained from the specimens fabricated using SCP versus those fabricated using FFF, respectively. The same PLA filament used for FFF was dissolved in chloroform and printed using the SCP with a tip of equal diameter to the FFF extruder nozzle. The SCP printed samples underwent more plastic deformation before failure, which occurred at a lower stress, than FFF printed samples. As shown in Figure 2d, the ratio of the ultimate tensile strength (UTS) in the cross-direction (CD) to the machine-direction (MD) (UTS_{CD}/UTS_{MD}) was significantly larger for SCP relative to FFF, specifically 0.85 \pm 0.10 versus 0.59 ± 0.07 , respectively (n = 10 samples for SCP; n = 8 samples for FFF). A relatively higher extent of visible layering artifacts (e.g., welds) was observed in the cross-sections of the FFF samples (SEM images are provided in Figure S1 of Supporting Information). Given a ratio of material properties in CD/MD (e.g., UTS_{CD}/UTS_{MD}) equal to one would indicate an isotropic material, the data suggest that the physics driving SCP mitigates some aspect of the printing artifacts or defects that cause material anisotropy in FFF with respect to UTS. In comparison, previous research on the anisotropic behavior of parts printed using FFF processes found UTS_{CD}/UTS_{MD} was 0.56 using acrylonitrile butadiene styrene, which was within

ACS Applied Materials & Interfaces

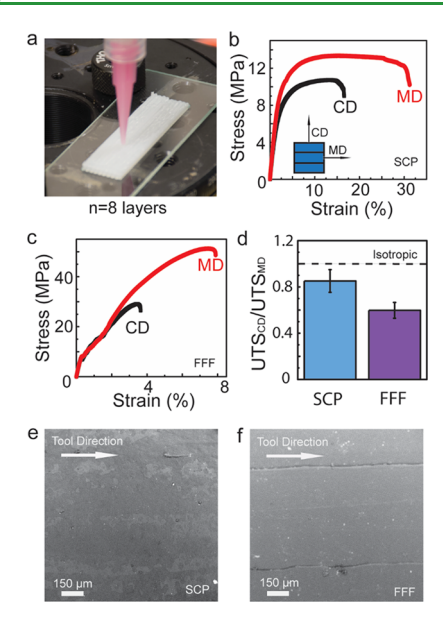


Figure 2. (a) Photograph of a multilayered PLA construct being fabricated via SCP (30 wt % PLA in chloroform solution). Representative tensile test results from the PLA test specimens fabricated via extrusion of polymer solutions (b) vs molten polymers (c) (i.e., SCP vs FFF). (d) Comparison of the anisotropy in UTS calculated as the ratio of the properties obtained when the stress was applied in the CD to the MD. Corresponding scanning electron micrographs of the test specimens printed using (e) SCP vs (f) FFF.

the standard deviation of the PLA samples we fabricated here using an FFF. 39 The value of UTS_{CD}/UTS_{MD} obtained for the SCP process also compares well with that obtained from other AM processes that utilize liquid-phase material systems, such as 1.07 obtained using a vat photopolymerization process (also commonly referred to as stereolithography). 42 It should also be noted that processing parameters have also been shown to affect bond quality among 3D printed molten thermoplastics, 43 which motivated our use of identical feed rates and material for tensile test specimen fabrication.

Having demonstrated that polymer solutions composed of an organic solvent can be used, we next examined the ability to utilize an aqueous-based polymer solution. The use of a waterbased polymer solution has the advantage of improved environmental friendliness, reduced potential chemical hazard to the user, and ability to utilize water-soluble thermoplastics via SCP. Poly(vinyl alcohol) (PVA), a water-soluble polymer, was selected as a test material given its ability to form mechanically robust thin films. 44,45 As shown in Figure S2 of Supporting Information, the UTS values of the MD samples were not significantly different from the CD samples. For example, we found the UTS for the MD and CD PVA samples were 41.9 \pm 5.2 and 53.5 \pm 12.1 MPa, respectively, (n = 5 samples each). These values compare reasonably with a previously reported value of 41 MPa for the UTS of cast PVA films. 46 These data support the observation in the chloroform— PLA system as well as provide evidence that the process is not restricted to a single thermoplastic-solvent system. Importantly, the use of the PVA-water system provides a second example regarding the fabrication of parts using highly viscous polymer solutions that otherwise pose technical challenges to jetting processes, which also commonly utilize solvent-based inks. In jetting processes, the Reynolds ($Re = \rho va/\eta$), Weber

 $(We = \rho v^2 a/\gamma)$, and Ohnesorge $(Oh = We^{0.5}/Re)$ numbers provide useful dimensionless groups for assessing material performance, where ρ , η , and γ are the density, dynamic viscosity, and surface tension of the fluid, respectively, ν is the velocity, and a is the characteristic length. ^{47,48} The inverse of the Ohnesorge number (Z = 1/Oh) has been utilized for characterizing droplet flow into three regimes: 49,50 (1) a viscous dissipation flow regime in which droplet ejection is prevented (Z < 1), (2) a stable droplet formation (1 < Z < 10), and (3) an unstable flow regime in which droplets are accompanied by additional satellite droplets (Z > 10). Given that η and γ for a 15 wt % solution are approximately 1000 cP and 30 dyn/cm, 51 Z is ~0.05 for the printed PLA and PVA solutions examined here, suggesting that they would not be processable using an inkjet printing process because of viscosity barriers. Thus, our results suggest that AM via microextrusion of polymer solutions relaxes the material property requirements relative to jetting processes, given the process does not require droplet formation. However, we note that while these results demonstrate that it is possible to fabricate thin films using highly viscous polymer solutions, viscosity and surface tension are important parameters that influence the rate of material spreading and contact angle of the filament with the substrate.

To assess the quality improvement observed in the SCP samples, we next examined the microstructure of the tensile test specimens using SEM. Figure 2e,f shows the SEM micrographs of the PLA samples printed via SCP and FFF, respectively. As shown in Figure 2f, the samples printed via FFF exhibit microgrooves parallel to the tool path direction (i.e., the MD) at the filament interfaces associated with a "rewelding" effect.^{27,34} The separation of the microgrooves compared reasonably to the specified layer in the FFF Gcode. Although such artifacts provide useful topographical cues in the case of scaffolds for tissue engineering, they cause anisotropy in mechanical properties of printed constructs as shown in Figure 2d.^{25,52} In contrast, as shown in Figure 2e, no microgrooves were visible in the SCP samples suggesting that the solidification processes of SCP and FFF exhibit different time scales (i.e., mass vs heat transfer processes, respectively). Given the data in Figure 2b-f suggest that SCP and FFF produce polymer constructs with different microstructure and mechanical properties, we next examined the effect of SCP on the relaxation (or swelling) dynamics of the thin films relative to control films fabricated by manual solution-cast methods (i.e., drop casting).

Figure 3a shows the time-resolved infrared spectra of liquid water diffusing into PLA films prepared via drop casting at 25 °C using a pellet form of amorphous PLA. The intensity of the infrared band associated with the O-H stretching of water (peak centered at ≈3400 cm⁻¹) increased with time, whereas the intensity of the infrared band associated with the CH3 stretching of PLA (peak centered at ≈1450 cm⁻¹) decreased. 53,54 Time-resolved spectra were collected every 2 min throughout the entire 24 h diffusion experiment. The increase in the O-H infrared band can be attributed to the diffusion of water, whereas the decrease in the CH₃ infrared band is representative of water-induced relaxation (or swelling) of the polymer and can be attributed to the nonequilibrium nature of the glassy PLA film. 53,55 Regression of the timeresolved Fourier transform infrared (FTIR) data for the CH₃ stretching infrared band from PLA to a three-element **ACS Applied Materials & Interfaces**

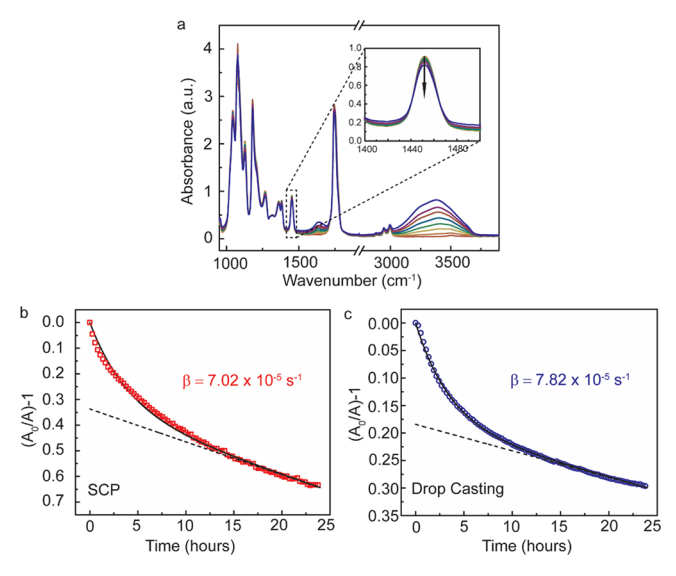


Figure 3. (a) Infrared spectra of liquid water diffusing into dry drop-cast PLA at 25 °C at selected time intervals. The inset shows the decrease of the CH_3 stretching band from PLA with time. Arrows indicate the direction of spectral change with time. Time-resolved absorbance data of the PLA CH_3 stretching as a function of time at 25 °C for films prepared via (b) SCP and (c) drop casting. Dashed lines represent a best-fit regression of the data to the late-time solution of eq 1, whereas solid lines represent a regression of the absorbance data to the full solution of eq 1, where relaxation time constant (β) was the only adjustable fitting parameter (for the sake of clarity, one-tenth of the data points used in the regression are shown in panels (b) and (c)).

viscoelastic relaxation model was used to quantify the film swelling response⁵³

$$\frac{A_0}{A(t)} - 1 = \frac{\sigma_0}{\eta}t + \frac{\sigma_0}{E}(1 - \exp(-\beta t)) \tag{1}$$

where A_0 and A(t) are the initial absorbance at time t=0 and the absorbance at time t, respectively, β is the relaxation (or swelling) time constant, and η and E are the film viscous and elastic parameters, respectively. More information regarding the relaxation model can be found elsewhere. 53,56,57

Figure 3b,c shows the regression of the PLA swelling data to both the late-time (as $t \to \infty$; black dashed line) and the full solution (black solid line) of eq 1 for the SCP versus drop-cast samples, respectively. The regression revealed that the relaxation time constant (β) was 7.02 \times 10⁻⁵ s⁻¹ for films created using SCP and $7.82 \times 10^{-5} \text{ s}^{-1}$ for the drop-cast films. We note that the same pellet form of amorphous PLA was used in both cases. As the relaxation time constants obtained from this analysis are a function of the thickness of the membrane, 57,58 these values were then "normalized" by the film thickness (74 \pm 2 μ m for SCP vs 61 \pm 5 μ m for drop casting) to allow for an accurate comparison between different films. This "normalized" relaxation constant (e.g., $\beta_{\text{norm}} = L^2 \times$ β) is representative of the "relaxation (swelling) speed" of the film, induced by the diffusion of water into the polymer. Performing this procedure revealed that the "normalized" relaxation time constants (β_{norm}) were 3.84 \times 10⁻⁸ cm²/s versus 2.91×10^{-8} cm²/s for the SCP and drop-cast films, respectively. This indicated that the SCP films responded more rapidly to the ingress of water as β_{norm} was approximately 33% larger for the SCP film relative to the film obtained from drop

casting. These results suggest that SCP leads to a relatively less frustrated nonequilibrium glassy state as compared to films created via manual drop casting.

Modeling of SCP Solidification Physics. Having shown that bonding defects are less pronounced in parts fabricated by SCP versus FFF and films fabricated using SCP offer reasonable transport properties relative to traditionally manufactured films, we next created a finite element model to understand the physics that drives the solidification process, specifically solidification due to loss of solvent from the printed object. Before examining the solidification process throughout the printing process using a numerical model, we calculated the Biot number (Bi), which compares the internal and external resistances to heat or mass transfer. Given the thermal conductivity (k) of a molten polymer is $0.3 \text{ W/m} \cdot \text{K}$, 59 the diffusivity of solvent in a polymer solution $(D_{\text{sol-poly}})$ is 3.36 \times 10^{-7} cm²/s (based on N,N-dimethylacetamide, DMAc), ⁶⁰ and the characteristic length of a polymer filament (L) is the sample thickness (1.5 mm), and assuming the convective heat and mass transfer coefficients (h and k_m , respectively) can be modeled based on flow across a flat plate, the Biot number for mass transfer $(Bi_{\rm m}=k_{\rm m}L/D_{\rm sol-poly})$ is significantly larger than the Biot number for heat transfer $(Bi_h = hL/k)$, suggesting that spatial effects (i.e., internal gradients) are more prominent in the SCP relative to the FFF. To understand the solidification physics of SCP, we constructed a moving boundary finite element model for calculating the solvent concentration in the part during printing. The associated mass transfer problem is described in Figure 4a in which solvent both diffuses within the

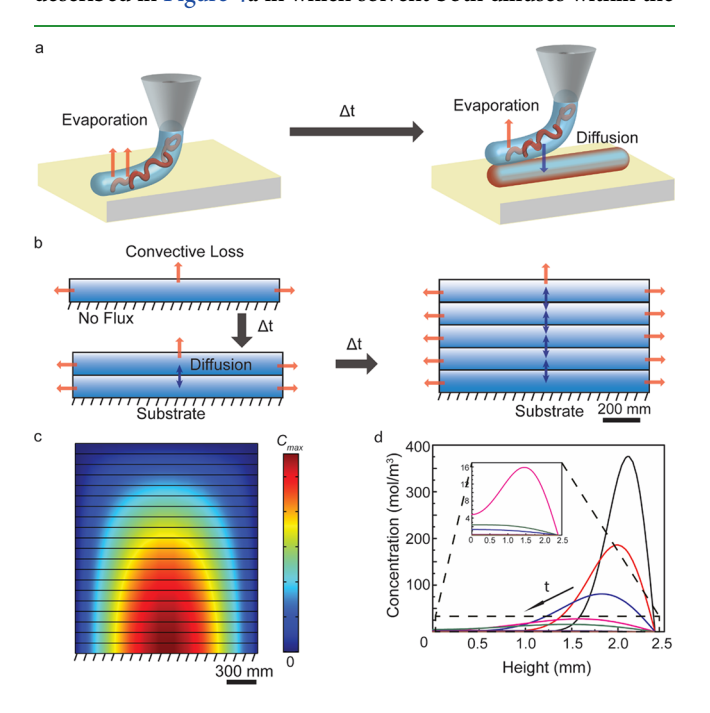


Figure 4. (a) Schematic highlighting the solidification mechanism associated with the SCP process, whereby a polymer solution solidifies into a polymer construct via evaporation. (b) Description of the moving boundary mass transfer model (hashed marks indicate the substrate). (c) Corresponding results of the finite element model described in panel (b) showing the concentration profile of solvent in a multilayer printed construct after drying for ~ 20 h (hashed marks indicate the substrate). (d) Spatiotemporal concentration profiles of solvent at the centerline of the part in panel (c) throughout the post-processing drying process.

ACS Applied Materials & Interfaces

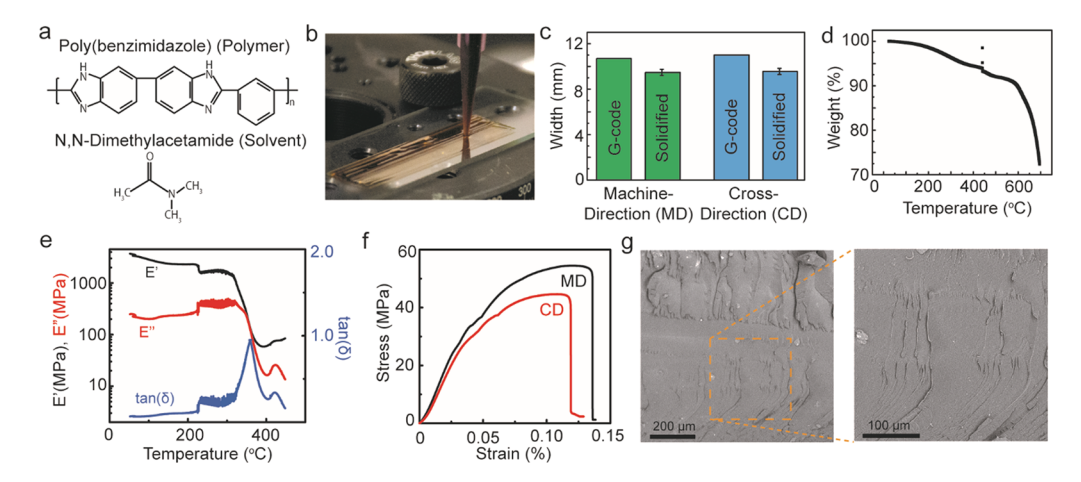


Figure 5. (a) Chemical structure of the PBI–DMAc polymer solution system. PBI has one of the highest glass-transition temperatures ($T_{\rm g}$) among polymers. (b) Photograph showing SCP of a multilayered PBI tensile test specimen. (c) Shrinkage of the fabricated part characterized by the size of the part after solidification compared to the programmed dimensions. (d) TGA showing decomposition ($T_{\rm d,95}$) of the printed PBI at 316 °C. (e) DMA of printed PBI showing $T_{\rm g}=358$ °C. (f) Tensile testing data showing comparable modulus of elasticity and UTS perpendicular and parallel to the direction of printing (i.e., the CD and MD, respectively). (g) Scanning electron micrograph of the PBI tensile test specimen fracture surface highlighting the high extent of interlayer bonding.

construct and is lost via convective transfer to the surroundings. As shown in Figure 4b, the model uses the solution from a previous stage with n layers as the initial condition for the subsequent stage that contains n + 1 layers. Figure 4c shows the concentration profile in a 20-layer printed construct after drying of the final layer ($t \sim 20$ h). It is noteworthy that the spatial concentration profile spans much greater than a single layer as predicted by $Bi_{\rm m} \gg 0.1$. Specifically, Figure 4d shows that the spatial concentration profile extends across the entire domain with the majority of mass distributed across 30-40% of the construct length scale. The predicted drying time based on the time for the solvent concentration in the first printed layer to reach zero was 16 h (see Figure 4d), which compared reasonably with the experimentally observed drying time of the 3D printed PBI samples. Thus, the results suggest that the printed polymer solution solidifies as a multilayered macroscopic assembly during the printing process. These calculations support the lack of observed defects and reduced anisotropy in UTS in the SCP versus the FFF samples (see Figure 2d-f).

Compatibility of SCP with High-Performance Thermoplastics. Having demonstrated that SCP produces constructs with greater isotropy in mechanical properties relative to FFF using a commonly printed material (PLA) as well as the use of low vapor pressure solvents (e.g., water), we next demonstrated the materials flexibility of SCP by printing a high-performance polymer that would pose technical challenges to FFF processes because of its high flow temperature. Many high-performance thermoplastics cannot be melt processed because thermal degradation will occur below the melt or flow temperatures, which limits the available high strength or functional materials for FFF. This fact has driven research in the area of composite materials for FFF. 61,62 PBI is a high-performance thermoplastic known for its high glasstransition temperature (T_g) , strength, and chemical stability and thus, is used in various applications across electronics and aerospace industries. 63 As shown in Figure 5a,b, we next used SCP to fabricate PBI test specimens. As shown in Figure 5b, we were able to fabricate PBI test specimens using the solvent DMAc, which has a vapor pressure approximately one order of magnitude lower than the water used for PVA printing. The data in Figure 5c show that the shrinkage during solidification of the SCP samples was relatively isotropic, suggesting that shrinkage effects could be incorporated as design considerations. The part shrinkages were 11.5 and 13% for the MD and the CD, respectively, relative to the tool path dimensions. We note that although the parts exhibit shrinkage, which is unavoidable because of the use of a solvent, the extent of shrinkage was comparable to that observed in other polymer AM processes.⁶⁴ Thermal gravimetric analysis (TGA) revealed a 5% degradation temperature ($T_{\rm d,95}$) of 316 °C, indicating a small amount of residual solvent (see Figure 5d). As shown in Figure 5e, dynamic mechanical analysis (DMA) showed T_g of the printed specimens was 358 °C by the tan (δ) method, which was lower than the vendor-reported value of 427 °C but still significantly higher than other available polymers for 3D printing. The samples exhibited a storage modulus greater than 1 GPa up to 323 °C, indicating stable mechanical properties at elevated temperatures. Similar to the PLA samples, the PBI samples also exhibited comparable strength along both axes (see Figure 5f and Figures S3 of Supporting Information). The PBI samples also showed fewer visible layering artifacts in the sample cross-sections relative to the samples made using FFF (SEM images provided in Figure S4 of Supporting Information). These results suggest that SCP is compatible with commonly 3D printed and high-performance thermoplastics (e.g., PLA and PBI, respectively) as well as solvents with vapor pressures ranging from 0.3–26.2 kPa (i.e., DMAc and chloroform, respectively), 65,66 suggesting that the ability to produce isotropic material properties is not restricted to a single thermoplastic-solvent system. We note that the reduced extent of layer-by-layer deposition defects observed in the PLA samples was also observed in the PBI samples. For example, scanning electron micrographs of the PBI fracture surfaces exhibited a high degree of roughness and nonuniform topographical features suggesting that the fracture did not result from the propagation of concentrated stress along an internal bond between adjacent layers (see Figure 5g).

Effect of Polymer Solution Concentration on Filament Cross-Sectional Profile and Resolution. The

requirement to melt polymers before printing in FFF not only restricts material selection but also limits the achievable resolution, which has implications in the resolution of spatial property control and blending of multiple materials. To estimate the minimum filament diameter achievable using continuous microextrusion printing processes, it is useful to consider the relationship between the pressure drop, pipe geometry, and fluid properties, commonly referred to as the Hagen—Poiseuille equation for the case of a Newtonian fluid. The corresponding relation for a power-law fluid (e.g., a molten polymer) flowing through a straight extruder nozzle is given as 67

$$\Delta p = \frac{2^{n+2} \left(\frac{3n+1}{n}\right)^n K L \overline{\nu}^n}{D^{n+1}} \tag{2}$$

where Δp is the pressure drop in the extruder nozzle, $\overline{\nu}$ is the average fluid velocity, L and D are the length and diameter of the nozzle, respectively, and n and K are the respective flow behavior and consistency indices of the fluid. Equation 2 can be rearranged to provide an estimate of the minimum extrudable feature size (D_{\min}) as:

$$D_{\min} = \left(\frac{2^{n+2} \left(\frac{3n+1}{n}\right)^n K L \overline{\nu}^n}{\Delta p}\right)^{1/n+1}$$
(3)

Considering the rheological properties of molten PLA ($K = 4.99 \times 10^3 \, \mathrm{Pa} \cdot \mathrm{s}^n$ and n = 0.75), ⁶⁸ the geometry of a typical FFF extruder nozzle ($L = 1 \, \mathrm{mm}$), a maximum available feed pressure (Δp_{max}) of 4000 psi, ⁶⁹ and $\overline{\nu}$ equals the minimum achievable feed rate for a typical FFF 3D printer (10 mm/s), the minimum feature size (D_{min}) for an extruded PLA filament is $D_{\mathrm{min}} = 109 \, \mu \mathrm{m}$. Alternatively, given a polymer solution exhibits a lower viscosity, SCP can surpass this minimum resolution of molten polymers as we show in Figure 6. Before examining the experimentally achievable minimum feature size, we first examined the effect of the polymer solution concentrations ranging from 2–30 wt % PLA in chloroform

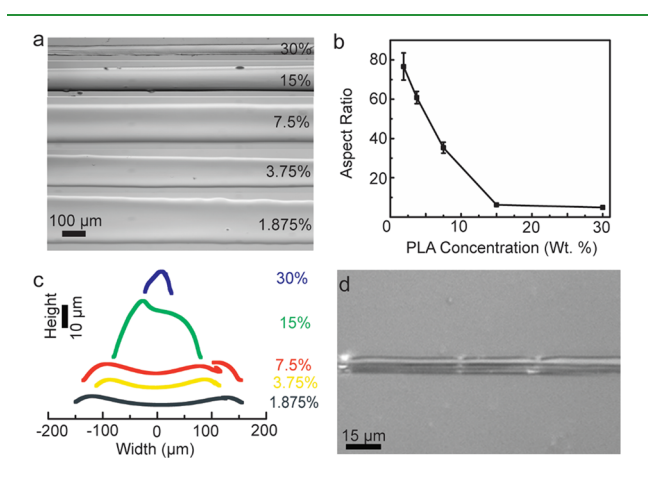


Figure 6. (a) Micrograph showing the effect of polymer solution (PLA) concentration in wt % on resultant filament width. Photographs correspond to solidified traces. (b) Effect of polymer solution concentration (PLA in chloroform) on the aspect ratio (width/height) of printed and solidified traces shown in panel (a). (c) Cross-sectional profiles corresponding to the data shown in panels (a) and (b). (d) Demonstration of the minimum printable feature size using the current SCP testbed (solidified filament diameter = 8.5 μ m).

on the dimensions of the printed filament. As shown in Figure 6a, we observed that polymer solutions of different concentration printed using the same parameters led to different filament widths. Although the extrusion pressure was set to create an extrudate (i.e., filament) of equal diameter to the nozzle, concentration-dependent ink behaviors, such as viscosity, surface tension, solidification time, and die swelling effects, can cause potential differences in volumetric flowrate. The relationship between deposited filament cross-sectional profile and concentration of the polymer solution was analyzed in terms of an aspect ratio, defined as the ratio of the filament width to height. Width and height data for the individual filaments are presented in Figure S5 of Supporting Information. As shown in Figure 6b, the dependence of filament aspect ratio on the polymer solution concentration exhibited nonlinear behavior up to a threshold concentration (15 wt % for the PLA-chloroform system) at which the filament aspect ratio approached a value of one. As shown in Figure 6c, SCP resulted in a range of concentration-dependent cross-sectional profiles. At low concentrations, the filaments exhibited a coffee ring-like effect in which mass accumulation was observed near the boundaries of the initially deposited filament. Coffee ring effects have also been previously observed in other solvent-based microextrusion- and jetting-based 3D printing applications, such as 3D printed electronics. 70,71 The most concentrated polymer solutions led to semicircular crosssection profiles typical of molten polymer traces, whereas the dilute polymer solutions led to relatively short and wide rectangular cross-sectional profiles. The data suggest SCP can offer unique opportunities for fabricating polymer constructs that exhibit filaments of aspect ratio and cross-sectional profile that are not achievable via FFF, such as in the emerging area of 3D printed microfluidics. 72-74

Given the most concentrated solutions exhibited the smallest solidified filament width as shown in Figure 6a-c, we next examined the minimum feature sizes that were possible to print using these formulations and our SCP testbed. As shown in Figure 6d, we found that it was possible to achieve a minimum filament width of 8.5 μ m using our SCP testbed. Although the resolution of SCP shown here surpasses the theoretical minimum feature size for FFF (109 μ m), theory suggests this resolution can be further reduced. For example, given $\overline{\nu} = 0.2$ mm/s, L = 1 mm, and $\Delta p_{\text{max}} = 100$ psi for SCP and assuming $K = 0.076 \text{ Pa} \cdot \text{s}^n$ and n = 1.0234 for a 15 wt %PLA solution,⁷⁵ eq 3 suggests that SCP could fabricate polymer constructs with nanoscale features ($D_{min} = 920 \text{ nm}$). Thus, this suggests that SCP could be used to control the spatial composition of thin film systems. Although the theoretical argument suggests the potential to create nanoscale features (e.g., topological or interfacial features), it does not consider the associated technical challenges that arise as the length scale associated with the printed and evaporating material decreases. Controlling the fluid flow field and the bulk concentration of the solvent vapor in the environment surrounding the 3D printed part will become important for quality printing applications. Although not examined here, the wettability of the polymer solution is also an important parameter to examine in future work as it affects potential filament retraction or spreading effects that may arise after printing. For example, low-wetting solution-substrate systems could potentially be used to prevent spreading of deposited polymer solution traces during solidification. We note that the ability to create polymer solutions with controlled retraction patterns after printing could also serve as an approach for reducing D_{\min} .

CONCLUSIONS

Here, we describe a new polymer AM process based on the continuous extrusion of polymer solutions, referred to as SCP. This manufacturing process differs from traditional polymer AM processes that utilize molten polymers (i.e., FFF). SCP offers various advantages compared to FFF, such as improved mechanical isotropy of printed films, compatibility with highperformance thermoplastics not usable with FFF, and minimum feature sizes that surpass FFF. Initial results from water swelling experiments indicate the potential for tuning the final transport properties of films created via SCP as the properties of these films differed from those created via manual drop casting. Future directions include the following: (1) improving our understanding of the physics that drive the formation of 3D features, such as overhangs, (2) dynamically modulating the solidification process through a real-time control of the evaporation process, (3) creating closed-loop controlled 3D printing approaches for fabrication with rapidly solidifying polymer solutions, and (4) creation of multimaterial thin film systems (e.g., composites). Ultimately, SCP enables high-resolution AM of a wide range of high-performance and functional polymer systems that are currently not printable, which has the potential to facilitate the design and fabrication of mechanically isotropic thin film systems and polymer constructs based on the principle of robotically directed solvent casting.

■ EXPERIMENTAL SECTION

Materials. Chloroform, DMAc, and PVA (MW = 130 kDa) were purchased from Sigma-Aldrich. PBI (26% in DMAc, S26 grade) was from Celazole. PLA for SCP and FFF studies was from Monoprice. PLA (grade 4060D; racemic mixture of L- and D-isomers; pellet form) for SCP and drop-casting studies was from NatureWorks, LLC. Ultrapure reverse osmosis water was obtained using a commercially available water purification system (resistivity ~18 MΩ; EMD Millipore).

Formulation and Preparation of Polymer Solutions for Printing. PLA was dissolved in chloroform overnight at room temperature to form a 30 wt % stock solution. Additional chloroform was added while stirring to dilute the solution to the desired final concentration. The vendor-provided 26 wt % solution of PBI in DMAc was used as a stock and was diluted by adding additional DMAc while magnetically stirring with gentle heating to achieve the desired concentration of 23 wt %, which was selected for optimized printability. PVA was dissolved in RO water by gentle heating at 90 °C for 60 min followed by cooling to 40 °C to form a 19% solution used for 3D printing.

Fabrication of Polymer Thin Films via Solvent-Cast 3D Printing. SCP was carried out using two custom microextrusion printing systems consisting of a three-axis motion control system (either a dispensing robot (F5200N; Fisnar) or a linear stage (AGS; Aerotech)), a digital pressure regulator (Ultimus V; Nordson), and a custom imaging system. The PLA, PBI, and PVA (n = 10, 10, and 10 samples, respectively) were fabricated using a fume hood to prevent the inhalation of volatile organic solvents. All samples were fabricated using the dispensing robot except for the high resolution printing, which was done using the linear stages. All samples were printed on PLA-coated glass slides to promote adhesion of the printed polymer solution.

FFF. FFF was performed using a commercially available plastic 3D printer (Monoprice Select V2; Monoprice). PLA samples were printed using a nozzle diameter of 0.4 mm, a layer height of 0.2 mm, a

printing speed of 80 mm/s, an extruder temperature of 245 °C, and a bed temperature of 95°C. The print time was approximately 3 min.

Tensile Testing Studies. Rectangular printed samples (11×40) × 1 mm) were used for tensile testing. PLA from Monoprice was printed via SCP using a 20 gauge-tapered tip, an extrusion pressure of 5-7 psi, and a printing speed of 6-7 mm/s. The build time was approximately 1 h. Following printing, the samples were dried in the fume hood. The PBI samples were printed using a 20 gauge-tapered tip (Nordson EFD), an extrusion pressure of 2.7-3.2 psi, and a printing speed of 6 mm/s. Following printing, the samples were soaked in water overnight to leach any remaining solvent from the part followed by drying at 100 °C for 2 h. The build time was approximately 2 h. The PVA samples were printed using an 18 gaugetapered tip (Nordson EFD), an extrusion pressure of 0.2 psi, and a printing speed of 3 mm/s. The build time was approximately 2 h. The samples were printed into two different groups that had orthogonal tool path directions, such that the applied load would be either perpendicular or parallel to the printed layers (see inset of Figure 2b) (i.e., the cross- and machine-direction, respectively). Tensile testing was done using a mechanical testing instrument (50 kN load cell; Model 3300; Instron) at a strain rate of 1 mm/min. Modulus was determined as the slope of the linear region of the stress-strain plot.

DMA. DMA was performed on SCP printed PBI samples ($5 \times 20 \times 1 \text{ mm}^3$) using a dynamic mechanical analyzer (Q800; TA Instruments). Measurements were made using a constant frequency and an amplitude of 1 Hz and 15 μ m, respectively. The temperature was swept from room temperature to 450 °C at a rate of 20 °C/min.

TGA. TGA was performed on the SCP printed PBI samples using a thermogravimetric analyzer (TGA550; TA Instruments). A heat rate of 20 $^{\circ}$ C/min was used from room temperature to 700 $^{\circ}$ C.

Profilometry. The cross-sectional profiles of the printed polymer filaments were characterized using a profilometer (DektakXT stylus profiler; Bruker; Billerica, MA). The profiles were acquired at a stylus force of 10 mg and a scan speed of 0.1 mm/s using a 12.5 μ m diamond conispherical stylus tip.

Finite Element Modeling. Studies were performed using commercially available FEA software (COMSOL Multiphysics, Version 5.3 a). The concentration profile in the printed construct during the printing process (i.e., layer-by-layer deposition) and throughout the post-processing drying interval was calculated by adapting a previously used model for calculating the transient concentration profiles in 3D printed pharmaceutical systems.⁷⁶ Mass transfer of solvent within the polymer construct was modeled using the Transport of Diluted Species interface within the Chemical Species Transport module. The computational domain was created using the graphical user interface based on the dimensions and shape of the test samples. Briefly, modeling of the evaporation-driven solidification process within the printed construct during fabrication requires solution of the diffusion equation across a computational domain that increases in size with time. The simulation began with analysis of the first printed layer. The initial concentration corresponded to the concentration of the printed solution. A convective flux boundary condition was implemented at the airpolymer interfaces of the construct, a flux continuity boundary condition was used at the interfaces between adjacent printed layers, and a no flux condition was used at the construct-substrate interface. The convective flux (j) was modeled using a form of Newton's Law of Cooling⁷

$$j = k_{\rm m}(c_{\rm s} - c_{\rm inf}) \tag{4}$$

where $k_{\rm m}$ is the convective mass transfer coefficient, $c_{\rm s}$ is the concentration of DMAc at the surface, and $c_{\rm inf}$ is the concentration of DMAc in the surrounding air (here, $c_{\rm inf}$ = 0 given SCP was performed in a fume hood). The value of $c_{\rm s}$ was calculated from the weight percentage of PBI in DMAc (23.4%), density of the PBI–DMAc solution (1021.9 kg/m³), and the molecular weight of DMAc (78 kDa). We used an empirical convective mass transfer correlation for a flat plate in parallel flow subjected to a constant surface concentration condition developed by Sieder and Tate to calculate the convective mass transfer coefficient⁷⁷

$$\overline{Sh} = 0.664Re^{1/2}Sc^{1/3} \tag{5}$$

where $\overline{Sh} = k_{\rm m} L_{\rm p}/D_{\rm DMAc\text{-}Air}$ is the average Sherwood number, $Re = \rho_{\rm a} v_{\rm a} L_{\rm p}/\mu_{\rm a}$ is the Reynolds number, and $Sc = \mu_{\rm a}/(\rho_{\rm a} D_{\rm DMAc\text{-}Air})$ is the Schmidt number (where $L_{\rm p}$ is the length of the plate, $D_{\rm DMAc\text{-}Air}$ is the diffusivity of DMAc in air, and $\mu_{\rm a}$, $\rho_{\rm a}$, and $\nu_{\rm a}$ are the respective viscosity, density, and velocity of air. The material properties were taken from previously published literature ($\mu_{\rm a} = 1.846 \times 10^{-5}~{\rm Pa\cdot s;}^{78}$ $\rho_{\rm a} = 1.177~{\rm kg/m}^3;^{78}~D_{\rm DMAc\text{-}Air} = 8 \times 10^{-6}~{\rm m}^2/{\rm s}).^{79}$ Values of $\nu_{\rm a}$ and $L_{\rm p}$ were obtained from the dimensions and flow rate of the fume hood and the size of the print stage for the SCP testbed. Calculations were done assuming Fickian diffusion within the solidifying construct, and the diffusion constant ($D_{\rm DMAc\text{-}Poly}$) of the DMAc in PBI was 3.36 $\times 10^{-11}~{\rm m}^2/{\rm s.}^{60}$

The computational domain was then discretized using a physicscontrolled mesh (extra fine element size), which consisted of 5200 domain and 1002 boundary elements. The concentration profile was obtained by solving the governing equations over a time interval equal to the time to print a single layer using a time step of 0.016 min. The resulting concentration profile was then stored. Proper density of the mesh was checked by examining convergence of the concentration by iterating from a fine to an extremely fine mesh size. Convergence was obtained using an extra fine mesh within 3.9% of the previous mesh. Subsequently, the computational domain was extended vertically by the addition of another subdomain to represent the addition of another printed layer of the construct. The governing equations were then resolved across the new computational domain for a duration of $t_{\rm p}$ subject to previously described boundary conditions but using a modified initial condition that included both the previously stored solution and the concentration profile corresponding to a new printed layer of concentrated polymer solution. This process was repeated n – 2 times, where n is the number of the printed layers (here, n = 20). Upon addition of the final layer, the time interval of the simulation was then extended into a post-processing interval of duration greater than $t_{\rm p}$ until the construct reached a bone-dry state.

Analysis of Part Microstructure. The dimensions of part microstructural features, such as filament or weld domains, shown in the light and scanning electron micrographs were quantified using an open-source image processing software (ImageJ; National Institutes of Health). The dimension of a given feature in pixels measured using the software line measurement tool was converted into units of micrometers using the image scale bar as a calibration scale.

Swelling Studies. For liquid water swelling experiments, timeresolved infrared spectra were collected using an FTIR spectrometer (Thermo Scientific Nicolet iS50R) equipped with a horizontal temperature-controlled attenuated total reflectance (ATR) cell (Specac Inc.). The spectra were collected using a liquid nitrogencooled mercury-cadmium-telluride detector at 32 scans per spectrum at a resolution of 4 cm⁻¹. For printed samples, a 10 wt % PLA in chloroform solution was printed onto a zinc selenide (ZnSe) attenuated total internal reflectance crystal using a 27 G-tapered tip (Nordson) at a speed of 4 mm/s and a pressure of 15 psi. For manually solution-cast samples (i.e., drop casting), a 5 wt % PLA in chloroform solution was pipetted directly onto the ZnSe crystal. For both preparation methods, the cast solution was then allowed to dry in a fume hood overnight, resulting in the formation of a thin film on the crystal. The polymer-coated ZnSe crystal was then placed in a vacuum oven at 65 °C for 2 h to remove any residual solvent. Transport experiments were conducted at 25 °C, controlled by a circulating water bath attached to the ATR flow cell. Time-resolved spectra were collected every 2 min throughout the entire 24 h diffusion experiment.

ASSOCIATED CONTENT

S Supporting Information

The Supporting Information is available free of charge on the ACS Publications website at DOI: 10.1021/acsami.8b22164.

Tensile testing studies and analysis of solidified filament cross-sectional profile (PDF)

AUTHOR INFORMATION

Corresponding Author

*E-mail: bnj@vt.edu. Tel: (540) 231-0755. Fax: (540) 231-3322.

ORCID ®

Eric M. Davis: 0000-0002-5633-5489 Blake N. Johnson: 0000-0003-4668-2011

Author Contributions

M.S. and A.P.H. conducted the microextrusion printing studies. M.S., A.P.H., Y.T., and E.C. conducted the mechanical testing studies. E.B. and R.J. conducted the water transport studies. M.S., A.P.H., Y.T., E.C., E.B., R.J., E.D., and B.N.J. contributed to data analysis. M.S., Y.T., and B.N.J. conducted the computational modeling. M.S., A.H., E.D., and B.N.J. conceived the studies. M.S., A.H., Y.T., E.C., E.D., and B.N.J. contributed to writing and editing of the manuscript.

Funding

National Science Foundation (grants CBET-1650601 and CPS-1739318).

Notes

The authors declare no competing financial interest.

ACKNOWLEDGMENTS

The authors are grateful for Zhenyu Kong, Andrew Law, David Hicks, and Carolina Tallon for technical support. B.N.J. is grateful for the generous support of the National Science Foundation (CBET-1650601 and CPS-1739318).

REFERENCES

- (1) Stuart, M. A. C.; Huck, W. T. S.; Genzer, J.; Müller, M.; Ober, C.; Stamm, M.; Sukhorukov, G. B.; Szleifer, I.; Tsukruk, V. V.; Urban, M.; Winnik, F.; Zauscher, S.; Luzinov, I.; Minko, S. Emerging Applications of Stimuli-Responsive Polymer Materials. *Nat. Mater.* **2010**, *9*, 101–113.
- (2) Jouault, N.; Zhao, D.; Kumar, S. K. Role of Casting Solvent on Nanoparticle Dispersion in Polymer Nanocomposites. *Macromolecules* **2014**, *47*, 5246–5255.
- (3) Jansto, A.; Davis, E. M. Role of Surface Chemistry on Nanoparticle Dispersion and Vanadium Ion Crossover in Nafion Nanocomposite Membranes. *ACS Appl. Mater. Interfaces* **2018**, *10*, 36385–36397.
- (4) Park, J.; Lee, S.; Lee, H. H. High-mobility Polymer Thin-film Transistors Fabricated by Solvent-assisted Drop-Casting. *Org. Electron.* **2006**, *7*, 256–260.
- (5) Farag, A. A. M.; Yahia, I. S. Structural, Absorption and Optical Dispersion Characteristics of Rhodamine B Thin Films Prepared by Drop Casting Technique. *Opt. Commun.* **2010**, 283, 4310–4317.
- (6) Nguyen, D. D.; Tai, N.-H.; Lee, S.-B.; Kuo, W.-S. Superhydrophobic and Superoleophilic Properties of Graphene-Based Sponges Fabricated Using a Facile Dip Coating Method. *Energy Environ. Sci.* **2012**, *5*, 7908–7912.
- (7) Mirri, F.; Ma, A. W. K.; Hsu, T. T.; Behabtu, N.; Eichmann, S. L.; Young, C. C.; Tsentalovich, D. E.; Pasquali, M. High-Performance Carbon Nanotube Transparent Conductive Films by Scalable Dip Coating. *ACS Nano* **2012**, *6*, 9737–9744.
- (8) Zhang, F.; Di, C.-a.; Berdunov, N.; Hu, Y.; Hu, Y.; Gao, X.; Meng, Q.; Sirringhaus, H.; Zhu, D. Ultrathin Film Organic Transistors: Precise Control of Semiconductor Thickness via Spin-Coating. *Adv. Mater.* **2013**, *25*, 1401–1407.

- (9) Krebs, F. C. Fabrication and Processing of Polymer Solar Cells: A Review of Printing and Coating Techniques. *Sol. Energy Mater. Sol. Cells* **2009**, 93, 394–412.
- (10) Liang, Y.; Xu, Z.; Xia, J.; Tsai, S.-T.; Wu, Y.; Li, G.; Ray, C.; Yu, L. For the Bright Future—Bulk Heterojunction Polymer Solar Cells with Power Conversion Efficiency of 7.4%. *Adv. Mater.* **2010**, 22, E135–E138.
- (11) Melchels, F. P. W.; Feijen, J.; Grijpma, D. W. A Review on Stereolithography and its Applications in Biomedical Engineering. *Biomaterials* **2010**, *31*, 6121–6130.
- (12) Ikuta, K.; Hirowatari, K.; Ogata, T. Three Dimensional Micro Integrated Fluid Systems (MIFS) Fabricated by Stereo Lithography. In Proceedings IEEE Micro Electro Mechanical Systems An Investigation of Micro Structures, Sensors, Actuators, Machines and Robotic Systems, Oiso, Japan, 25–28 Jan 1994; IEEE: Piscataway, NJ, 1994; pp 1–6.
- (13) Pede, D.; Serra, G.; De Rossi, D. Microfabrication of Conducting Polymer Devices by Ink-Jet Stereolithography. *Mater. Sci. Eng. C* **1998**, *5*, 289–291.
- (14) Pham, T. A.; Kim, D.-P.; Lim, T.-W.; Park, S.-H.; Yang, D.-Y.; Lee, K.-S. Three-Dimensional SiCN Ceramic Microstructures via Nano-Stereolithography of Inorganic Polymer Photoresists. *Adv. Funct. Mater.* **2006**, *16*, 1235–1241.
- (15) Zhang, X.; Jiang, X. N.; Sun, C. Micro-Stereolithography of Polymeric and Ceramic Microstructures. *Sens. Actuators, A* **1999**, 77, 149–156.
- (16) Lu, Y.; Chen, S. C. Micro and Nano-Fabrication of Biodegradable Polymers for Drug Delivery. *Adv. Drug Deliv. Rev.* **2004**, *56*, 1621–1633.
- (17) Park, S.-H.; Yang, D.-Y.; Lee, K.-S. Two-Photon Stereolithography for Realizing Ultraprecise Three-dimensional Nano/ Microdevices. *Laser Photonics Rev.* **2009**, *3*, 1–11.
- (18) Bikas, H.; Stavropoulos, P.; Chryssolouris, G. Additive Manufacturing Methods and Modelling Approaches: A Critical Review. *Int. J. Adv. Manuf. Technol.* **2016**, 83, 389–405.
- (19) Vaezi, M.; Seitz, H.; Yang, S. A Review on 3D Micro-Additive Manufacturing Technologies. *Int. J. Adv. Manuf. Technol.* **2013**, *67*, 1721–1754.
- (20) Singh, M.; Haverinen, H. M.; Dhagat, P.; Jabour, G. E. Inkjet Printing—Process and Its Applications. *Adv. Mater.* **2010**, *22*, *673*–685.
- (21) Lu, Z.; Layani, M.; Zhao, X.; Tan, L. P.; Sun, T.; Fan, S.; Yan, Q.; Magdassi, S.; Hng, H. H. Fabrication of Flexible Thermoelectric Thin Film Devices by Inkjet Printing. *Small* **2014**, *10*, 3551–3554.
- (22) Sele, C. W.; von Werne, T.; Friend, R. H.; Sirringhaus, H. Lithography-Free, Self-Aligned Inkjet Printing with Sub-Hundred-Nanometer Resolution. *Adv. Mater.* **2005**, *17*, 997–1001.
- (23) Lewis, J. A. Direct Ink Writing of 3D Functional Materials. *Adv. Funct. Mater.* **2006**, *16*, 2193–2204.
- (24) Low, Z.-X.; Chua, Y. T.; Ray, B. M.; Mattia, D.; Metcalfe, I. S.; Patterson, D. A. Perspective on 3D printing of Separation Membranes and Comparison to Related Unconventional Fabrication Techniques. *J. Membr. Sci.* **2017**, *523*, 596–613.
- (25) Ahn, S.-H.; Montero, M.; Odell, D.; Roundy, S.; Wright, P. K. Anisotropic Material Properties of Fused Deposition Modeling ABS. *Rapid Prototyp. J.* **2002**, *8*, 248–257.
- (26) Lee, C. S.; Kim, S. G.; Kim, H. J.; Ahn, S. H. Measurement of Anisotropic Compressive Strength of Rapid Prototyping Parts. *J. Mater. Process. Technol.* **2007**, *187*–*188*, 627–630.
- (27) Sood, A. K.; Ohdar, R. K.; Mahapatra, S. S. Experimental Investigation and Empirical Modelling of FDM Process for Compressive Strength Improvement. *J. Adv. Res.* **2012**, *3*, 81–90.
- (28) Roberson, D.; Shemelya, C. M.; MacDonald, E.; Wicker, R. Expanding the Applicability of FDM-Type Technologies through Materials Development. *Rapid Prototyp. J.* **2015**, *21*, 137–143.
- (29) Masood, S. H.; Song, W. Q. Development of New Metal/Polymer Materials for Rapid Tooling Using Fused Deposition Modelling. *Mater. Des.* **2004**, *25*, 587–594.
- (30) Wong, K. V.; Hernandez, A. A Review of Additive Manufacturing. ISRN Mech. Eng. 2012, 2012, 208760.

- (31) Tanikella, N. G.; Wittbrodt, B.; Pearce, J. M. Tensile Strength of Commercial Polymer Materials for Fused Filament Fabrication 3D printing. *Addit. Manuf.* **2017**, *15*, 40–47.
- (32) Ly, S. T.; Kim, J. Y. 4D Printing Fused Deposition Modeling Printing with Thermal-Responsive Shape Memory Polymers. *Int. J. Precis. Eng. Manuf.-Green Technol.* **2017**, *4*, 267–272.
- (33) Ligon, S. C.; Liska, R.; Stampfl, J.; Gurr, M.; Mülhaupt, R. Polymers for 3D Printing and Customized Additive Manufacturing. *Chem. Rev.* **2017**, *117*, 10212–10290.
- (34) Bellehumeur, C.; Li, L.; Sun, Q.; Gu, P. Modeling of Bond Formation Between Polymer Filaments in the Fused Deposition Modeling Process. *J. Manuf. Process* **2004**, *6*, 170–178.
- (35) McIlroy, C.; Olmsted, P. D. Disentanglement Effects on Welding Behaviour of Polymer Melts during the Fused-filament-fabrication Method for Additive Manufacturing. *Polymer* **2017**, *123*, 376–391.
- (36) Seppala, J. E., Hillgartner, K. E., Davis, C. S., Migler, K. D. Thermography and Weld Strength Characterization of Thermoplastic Extrusion 3D Printing. In *SPE ANTEC 2016*, Indianapolis, IN, 23–25 May 2016; SPE: Bethel, CT, 2016.
- (37) Ning, F.; Cong, W.; Qiu, J.; Wei, J.; Wang, S. Additive Manufacturing of Carbon Fiber Reinforced Thermoplastic Composites using Fused Deposition Modeling. *Composites, Part B* **2015**, *80*, 369–378.
- (38) Nikzad, M.; Masood, S. H.; Sbarski, I.; Groth, A. M. Rheological Properties of a Particulate-Filled Polymeric Composite through Fused Deposition Process. *Mater. Sci. Forum* **2010**, *654*–*656*, 2471–2474.
- (39) Ziemian, C.; Sharma, M.; Ziemian, S. Anisotropic Mechanical Properties of ABS Parts Fabricated by Fused Deposition Modelling; INTECH Open Access Publisher: London, 2012.
- (40) Vaezi, M.; Yang, S. Freeform Fabrication of Nanobiomaterials Using 3D Printing. In *Rapid Prototyping of Biomaterials*; Narayan, R., Ed.; Woodhead Publishing: London, 2014; pp 16–74.
- (41) Ghosh, S.; Parker, S. T.; Wang, X.; Kaplan, D. L.; Lewis, J. A. Direct-Write Assembly of Microperiodic Silk Fibroin Scaffolds for Tissue Engineering Applications. *Adv. Funct. Mater.* **2008**, *18*, 1883–1889
- (42) Naik, D. L.; Kiran, R. On Anisotropy, Strain Rate and Size Effects in Vat Photopolymerization Based Specimens. *Addit. Manuf.* **2018**, 23, 181–196.
- (43) Sun, Q.; Rizvi, G. M.; Bellehumeur, C. T.; Gu, P. Effect of Processing Conditions on the Bonding Quality of FDM Polymer Filaments. *Rapid Prototyp. J.* **2008**, *14*, 72–80.
- (44) Lin, J.-H.; Lin, Z.-I.; Pan, Y.-J.; Hsieh, C.-T.; Huang, C.-L.; Lou, C.-W. Thermoplastic Polyvinyl Alcohol/Multiwalled Carbon Nanotube Composites: Preparation, Mechanical Properties, Thermal Properties, and Electromagnetic Shielding Effectiveness. *J. Appl. Polym. Sci.* 2016, 133, 43474.
- (45) Zhao, X.; Zhang, Q.; Chen, D.; Lu, P. Enhanced Mechanical Properties of Graphene-Based Poly(vinyl alcohol) Composites. *Macromolecules* **2010**, 43, 2357–2363.
- (46) Chen, C.-h.; Torrents, A.; Kulinsky, L.; Nelson, R. D.; Madou, M. J.; Valdevit, L.; LaRue, J. C. Mechanical Characterizations of Cast Poly(3,4-ethylenedioxythiophene):Poly(styrenesulfonate)/Polyvinyl Alcohol Thin Films. *Synth. Met.* **2011**, *161*, 2259–2267.
- (47) Derby, B. Inkjet Printing of Functional and Structural Materials: Fluid Property Requirements, Feature Stability, and Resolution. *Annu. Rev. Mater. Res.* **2010**, *40*, 395–414.
- (48) Derby, B. Inkjet Printing Ceramics: From Drops to Solid. J. Eur. Ceram. Soc. 2011, 31, 2543–2550.
- (49) Fromm, J. E. Numerical Calculation of the Fluid Dynamics of Drop-on-Demand Jets. *IBM J. Res. Dev.* **1984**, *28*, 322–333.
- (50) Reis, N.; Derby, B. Ink Jet Deposition of Ceramic Suspensions: Modeling and Experiments of Droplet Formation. MRS Online Proc. Libr. 2000, 625, 117.
- (51) Casasola, R.; Thomas, N. L.; Trybala, A.; Georgiadou, S. Electrospun Poly Lactic Acid (PLA) fibres: Effect of Different Solvent

- Systems on Fibre Morphology and Diameter. *Polymer* **2014**, 55, 4728–4737.
- (52) Zou, R.; Xia, Y.; Liu, S.; Hu, P.; Hou, W.; Hu, Q.; Shan, C. Isotropic and Anisotropic Elasticity and Yielding of 3D Printed Material. *Composites, Part B* **2016**, *99*, 506–513.
- (53) Davis, É. M.; Theryo, G.; Hillmyer, M. A.; Cairncross, R. A.; Elabd, Y. A. Liquid Water Transport in Polylactide Homo and Graft Copolymers. *ACS Appl. Mater. Interfaces* **2011**, *3*, 3997–4006.
- (54) Zhang, J.; Tsuji, H.; Noda, I.; Ozaki, Y. Structural Changes and Crystallization Dynamics of Poly(L-lactide) during the Cold-Crystallization Process Investigated by Infrared and Two-Dimensional Infrared Correlation Spectroscopy. *Macromolecules* **2004**, *37*, 6433–6439
- (55) Davis, E. M.; Minelli, M.; Giacinti Baschetti, M.; Elabd, Y. A. Non-Fickian Diffusion of Water in Polylactide. *Ind. Eng. Chem. Res.* **2013**, *52*, 8664–8673.
- (56) Hallinan, D. T. Jr.; De Angelis, M. G.; Giacinti Baschetti, M.; Sarti, G. C.; Elabd, Y. A. Non-Fickian Diffusion of Water in Nafion. *Macromolecules* **2010**, *43*, 4667–4678.
- (57) Davis, E. M.; Benetatos, N. M.; Regnault, W. F.; Winey, K. I.; Elabd, Y. A. The Influence of Thermal History on Structure and Water Transport in Parylene C Coatings. *Polymer* **2011**, *52*, 5378–5386
- (58) Davis, E. M.; Stafford, C. M.; Page, K. A. Elucidating Water Transport Mechanisms in Nafion Thin Films. *ACS Macro Lett.* **2014**, 3, 1029–1035.
- (59) Jean-Fulcrand, A.; Masen, M. A.; Bremner, T.; Wong, J. S. S. High Temperature Tribological Properties of Polybenzimidazole (PBI). *Polymer* **2017**, *128*, 159–168.
- (60) Li, G.; Kawatake, K.-i.; Li, X.; Yamada, T.; Tada, K.; Katsuo, K.-i.; Ishihara, H. Measurement of Diffusion Coefficients of Dimethyl Formamide and Dimethyl Acetamide in Segmented Poly (urethaneurea). *Seikei-Kakou* **2006**, *18*, 517–523.
- (61) de Leon, A. C.; Chen, Q.; Palaganas, N. B.; Palaganas, J. O.; Manapat, J.; Advincula, R. C. High Performance Polymer Nanocomposites for Additive Manufacturing Applications. *React. Funct. Polym.* **2016**, *103*, 141–155.
- (62) Wang, X.; Jiang, M.; Zhou, Z.; Gou, J.; Hui, D. 3D Printing of Polymer Matrix Composites: A Review and Prospective. *Composites, Part B* **2017**, *110*, 442–458.
- (63) Xiao, L.; Zhang, H.; Jana, T.; Scanlon, E.; Chen, R.; Choe, E.-W.; Ramanathan, L. S.; Yu, S.; Benicewicz, B. C. Synthesis and Characterization of Pyridine-Based Polybenzimidazoles for High Temperature Polymer Electrolyte Membrane Fuel Cell Applications. *Fuel Cells* **2005**, *5*, 287–295.
- (64) Hegde, M.; Meenakshisundaram, V.; Chartrain, N.; Sekhar, S.; Tafti, D.; Williams, C. B.; Long, T. E. 3D Printing All-Aromatic Polyimides using Mask-Projection Stereolithography: Processing the Nonprocessable. *Adv. Mater.* **2017**, *29*, 1701240.
- (65) Philippe, R.; Jambon, C.; Clechet, P. Thermodynamic Properties of Dimethylsulfoxide + Halomethane Mixtures II. Vapour Pressures and Excess Thermodynamic Functions. *J. Chem. Thermodyn.* **1973**, *5*, 431–444.
- (66) Nasirzadeh, K.; Neueder, R.; Kunz, W. Vapor Pressures of Propylene Carbonate and N,N-Dimethylacetamide. J. Chem. Eng. Data **2005**, 50, 26–28.
- (67) McCabe, W. L.; Smith, J. C.; Harriott, P. Unit Operations of Chemical Engineering, 7th ed.; McGraw-Hill: New York, 2005.
- (68) Djellali, S.; Sadoun, T.; Haddaoui, N.; Bergeret, A. Viscosity and Viscoelasticity Measurements of Low Density Polyethylene/poly(lactic acid) Blends. *Polym. Bull.* **2015**, *72*, 1177–1195.
- (69) Go, J.; Schiffres, S. N.; Stevens, A. G.; Hart, A. J. Rate Limits of Additive Manufacturing by Fused Filament Fabrication and Guidelines for High-throughput System Design. *Addit. Manuf.* **2017**, *16*, 1–11.
- (70) Soltman, D.; Subramanian, V. Inkjet-Printed Line Morphologies and Temperature Control of the Coffee Ring Effect. *Langmuir* **2008**, 24, 2224–2231.

- (71) Kong, Y. L.; Tamargo, I. A.; Kim, H.; Johnson, B. N.; Gupta, M. K.; Koh, T.-W.; Chin, H.-A.; Steingart, D. A.; Rand, B. P.; McAlpine, M. C. 3D Printed Quantum Dot Light-Emitting Diodes. *Nano Lett.* **2014**, *14*, 7017–7023.
- (72) Singh, M.; Tong, Y.; Webster, K.; Cesewski, E.; Haring, A. P.; Laheri, S.; Carswell, B.; O'Brien, T. J.; Aardema, C. H.; Senger, R. S.; Robertson, J. L.; Johnson, B. N. 3D Printed Conformal Microfluidics for Isolation and Profiling of Biomarkers from Whole Organs. *Lab Chip* **2017**, *17*, 2561–2571.
- (73) Cesewski, E.; Haring, A. P.; Tong, Y.; Singh, M.; Thakur, R.; Laheri, S.; Read, K. A.; Powell, M. D.; Oestreich, K. J.; Johnson, B. N. Additive Manufacturing of Three-dimensional (3D) Microfluidic-Based Microelectromechanical Systems (MEMS) for Acoustofluidic Applications. *Lab Chip* 2018, *18*, 2087–2098.
- (74) Johnson, B. N.; Lancaster, K. Z.; Hogue, I. B.; Meng, F.; Kong, Y. L.; Enquist, L. W.; McAlpine, M. C. 3D Printed Nervous System on a Chip. *Lab Chip* **2016**, *16*, 1393–1400.
- (75) Suresh, K.; Boro, R.; Kumar, R. V.; Pugazhenthi, G. Effect of Concentration and Temperature on Rheological Behaviour of Polystyrene Solution. *Macromol. Symp.* **2016**, *362*, 87–100.
- (76) Haring, A. P.; Tong, Y.; Halper, J.; Johnson, B. N. Programming of Multicomponent Temporal Release Profiles in 3D Printed Polypills via Core—Shell, Multilayer, and Gradient Concentration Profiles. *Adv. Healthcare Mater.* **2018**, *7*, 1800213.
- (77) Incropera, F. P.; DeWitt, D. P. Fundamentals of Heat and Mass Transfer, 3rd ed.; John Wiley & Sons: Hoboken, NJ, 2002.
- (78) Neutrium. Properties of Air. https://neutrium.net/properties/properties-of-air/ (accessed Dec 19, 2018).
- (79) Chemical Update Worksheet: N,N-Dimethylacetamide. Department of Environmental Quality, State of Michigan: Warren, MI, 2015.